Electronic Supplementary Material (ESI) for Materials Horizons.

Semi-paracrystallinity in semi-conducting polymers

Sara Marina,[a] Edgar Gutierrez-Fernandez,[a] Junkal Gutierrez,[bc] Marco Gobbi,[de] Nicolás Ramos,[a] Eduardo Solano,[f] Jeromy Rech,[g] Wei You, [g] Luis Hueso,[d] Agnieszka Tercjak, [b] Harald Ade, * [h] and Jaime Martin * [aij]

[a.] *POLYMAT, University of the Basque Country UPV/EHU Av. de Tolosa 72, 20018, Donostia-San Sebastián, Spain*
[b.] *Group 'Materials + Technologies', Faculty of Engineering Guipuzcoa, University of the Basque Country (UPV/EHU), Plaza Europa 1, 20018 Donostia, Spain.*
[c.] *Faculty of Engineering Vitoria-Gasteiz, University of the Basque Country (UPV/EHU), C/Nieves Cano 12, 01006 Vitoria-Gasteiz, Spain*
[d.] *CIC nanoGUNE BRTA, 20018 Donostia-San Sebastian, Basque Country, Spain. IKERBASQUE, Basque Foundation for Science, 48013 Bilbao, Basque Country, Spain.*
[e.] *Centro de Física de Materiales CFM-MPC (CSIC-UPV/EHU), 20018 Donostia-San Sebastian, Basque Country, Spain*
[f.] *ALBA Synchrotron Light Source, NCD-SWEET Beamline, 08290 Cerdanyola del Vallès, Spain*
[g.] *Department of Chemistry, University of North Carolina at Chapel Hill, Chapel Hill, North Carolina, 27599, USA*
[h.] *Department of Physics and Organic and Carbon Electronics Laboratories (ORaCEL), North Carolina State University, Raleigh, NC, 27695 USA. E-mail hwade@ncsu.edu*
[i.] *Universidade da Coruña, Grupo de Polímeros, Centro de Investigacións Tecnolóxicas (CIT), Esteiro, 15471 Ferrol, Spain*
[j.] *Ikerbasque, Basque Foundation for Science, 48013 Bilbao, Spain. E-mail jaime.martin.perez@udc.es*

Paracrystalline model:

According to IUPAC, paracrystallinity is a crystal model characterized by lattice distortions and hence by limited order along given lattice directions. Long-range lattice, cumulative distortions are produced by statistically homogeneous disturbances to an ideal crystalline lattice [1]). To measure the statistical fluctuations of local arrangement of atoms (lattice spacings), the paracrystalline distortion parameter, g, was introduced. g is the ratio of statistical fluctuations Δa_{ik} of a lattice vector a_i along the direction a_k.

$$g_{ik} = \frac{\Delta a_{ik}}{a_k}$$

g-values range between 0 for a distortion-free crystal to 1 for a Boltzmann gas, being 0.03 a typical value for a semicrystalline polymer and 0.07 - 0.12 the g-value of a para-crystalline lattice. [2]

g-parameter can be extracted using formalisms that allow to separate the different contributions to the breath of diffraction peaks, such as the Williamson-Hall [3]and the Warren Averbach[4] methods. Recently, Rivnay et al. have proposed that for highly disordered system (where the x-ray coherence length is determined solely by lattice disorder), the g-parameter can be readily extracted from the width of the first order diffraction peak[1, 5] as

$$g_{ik} = \sqrt{\frac{\Delta q}{2\pi q_0}}$$

where q_0 the maximum peak position and Δq the full width half maximum of the peak"

1. J. Rivnay, R. Noriega, R. J. Kline, A. Salleo and M. F. Toney, *Phys. Rev. B*, 2011, **84**.
2. A. M. Hindeleh and R. Hosemann, *J Mater Sci*, 1991, **26**, 5127-5133.
3. G. K. Williamson and W. H. Hall, *Acta Metallurgica*, 1953, **1**, 22-31.
4. B. E. Warren and B. L. Averbach, *Journal of Applied Physics*, 1950, **21**, 595-599.
5. R. Noriega, J. Rivnay, K. Vandewal, F. P. V. Koch, N. Stingelin, P. Smith, M. F. Toney and A. Salleo, *Nature Materials*, 2013, **12**, 1038.
6. J. Martín, N. Stingelin and D. Cangialosi, *The Journal of Physical Chemistry Letters*, 2018, **9**, 990-995.

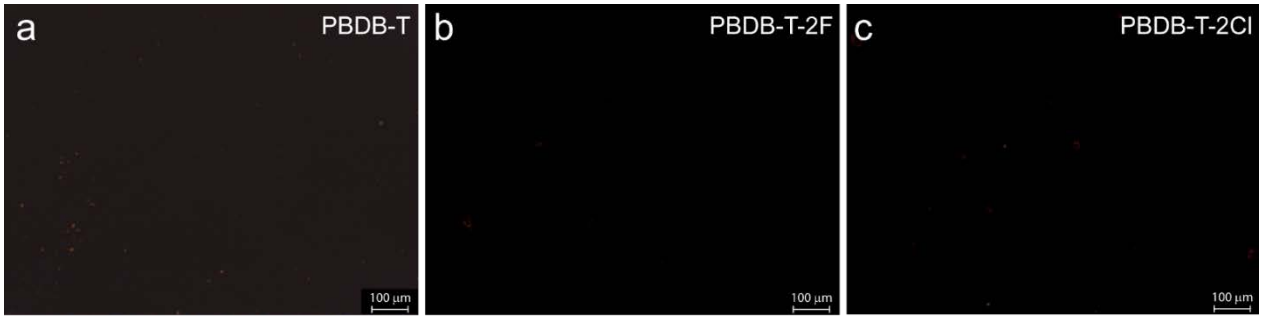

Figure S1. Polarized optical microscopy (POM) images of spin cast polymer films (from a 20 mg·mL^{-1} chlorobenzene solution) (a) PBDB-T, (b) PBDB-T-2F and (c) PBDB-T-2Cl. The width of the micrographs corresponds to 100 µm.

Spin-cast polymer samples were evaluated by polarized optical microscopy (POM). Samples were directly spin casted on glass from. The glass slide was placed between the polarizer and the orthogonally oriented analyzer of a bright-field optical microscope (Zeiss Axio Scope A1) equipped with a 10X objective and a tungsten-halogen bulb.

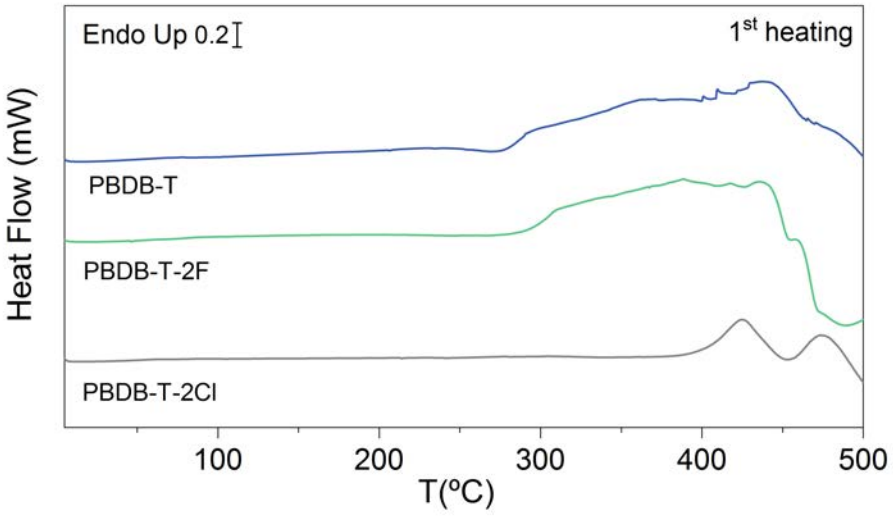

Figure S2. Conventional differential scanning calorimetry thermograms collected during a heating ramp from 0 ºC up to 500 °C at 20 °C·min^{-1} (a) PBDB-T, and (b) PBDB-T-2F and (c) PBDB-T-2Cl.

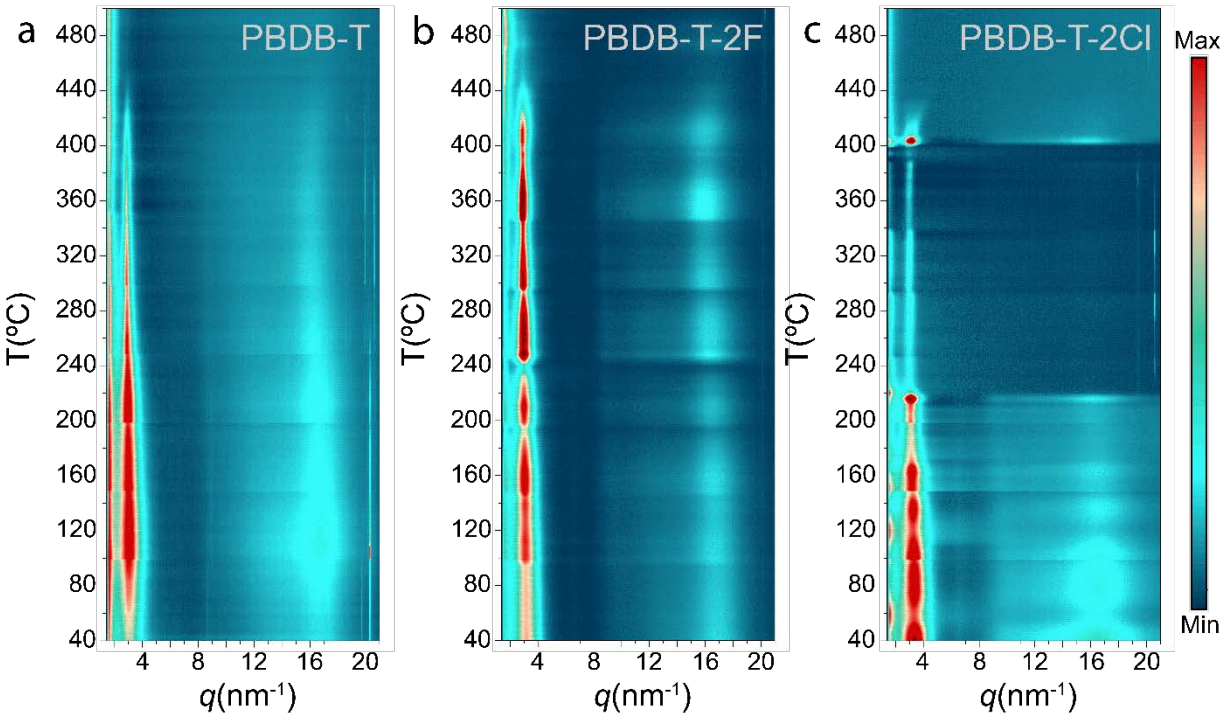

Figure S3. Contour plot of *azimuthal* integrations 2D GIWAXS patterns collected during a heating ramp from 30 °C up to 500 °C at 20 °C·min^{-1} (a) PBDB-T, and (b) PBDB-T-2F and (c) PBDB-T-2Cl.

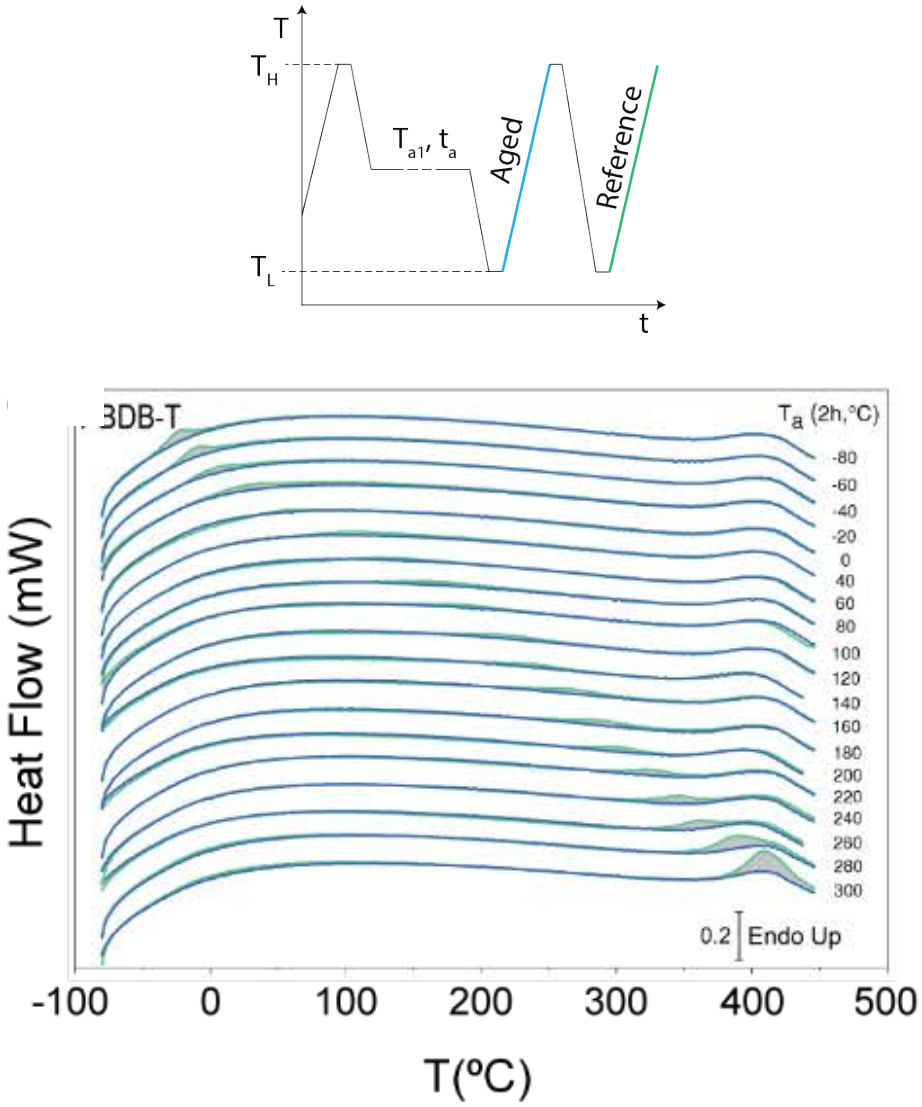

Figure S4. Aging thermal protocol applied (top panel) and results (bottom panel) of the FSC experiments conducted to identify the thermal (thermotropic behaviour) of PBDB-T spin cast films [6]. Green curves correspond to the heating traces (at 4000 ºC·s^{-1}) after ageing samples for 2 h at the temperatures indicated on the right-hand side of each curve. Cooling and heating rates were 4000 ºC·s^{-1}.

Analysis of the enothermic order-disorder transition

It should be noted that compared to regular DSC, FSC allows for the application of much faster scanning rates (scanning rates of 4000 °C·s^{-1} were applied in our experiments), which on the one hand prevents thermal degradation of compounds at high temperatures,

thereby enabling the detection of order-disorder transitions, and, on the other hand, allow to probe spin cast films that can be safely correlated with GIWAXS data (and device data).

Indeed, in order to rule out that this endothermic peak is due to degradation, we cycled a PBDB-T film between between -90 and 450 ºC (i.e. above the endothermic peak) and recorded heating traces were compared (Figure S5 in the Supporting Information). Because the heat flow values measured are exactly equal in all those heating, we conclude that (i) the mass of material does not change during the experiment and (ii) the specific heat capacity (cp) of the material does not change during the experiment; thus confirming the absence of any thermal degradation.

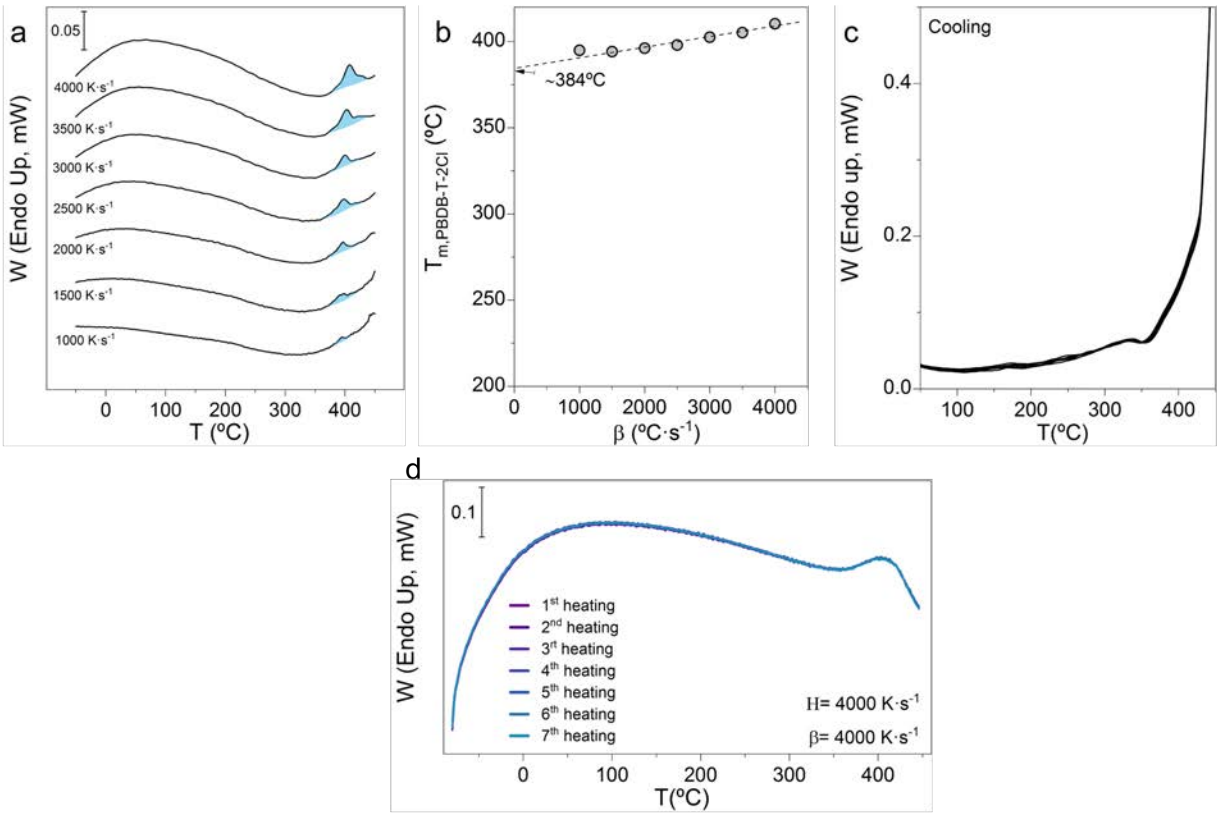

Figure S5. (a) FSC heating thermograms of PBDB-T-2Cl at different heating rates (respective heating rates are depicted in the plot). (b) PBDB-T-2Cl melting temperature, $T_{m,PBDB\text{-}T\text{-}2Cl}$, as a function of the heating rate. (c) cooling scans at 4000 °C·s^{-1} after the heating scans in a). (d) Multiple heating scans of PBDB-T films recorded at 4000 °C·s^{-1} after quenching the film at 4000 °C·s^{-1}.

The scanning rates applied in the FSC experiments are selected according to the compromise between recording a reasonable intensity of the calorimetric signals (which escalates with the scanning rate), avoiding the degradation of the material at high-temperatures (which is minimized for fast scanning rates) and minimizing the thermal lag (which results from the fast scanning rates).

In order to evaluate these points we conducted the following experiments: a spin cast PBDB-T-2Cl film was thermally cycled from -50 to 450 ºC. In a first experiment, applied heating rates ranged between 1000 °C·s^{-1} and 4000 °C·s^{-1} and cooling rate was in all cases 4000 °C·s^{-1}. Results are shown in Figure S5a, S5b and S5c. These data showed that: (1) the applied heating rates must be 2000 °C·s^{-1} or higher in order to observe clear melting peaks (Figure S5a); (2) Thermal lag is relatively small – less than 20 ºC- even for the fastest heating rates and (Figure S5b) (3) no significant degradation is detected because cooling traces overlap despite the sample had been heated at different rates (Figure S5c). In order to confirm the absence of degradation, a second experiment was conducted in which a spin cast PBDB-T-2Cl film was thermally cycled 7 times from -50 to 450 ºC at heating and cooling rates of 4000 °C·s^{-1}. Figure S5d shows that all the 7 heating traces completely overlap, which rules out the degradation of the polymer during the experiment. In conclusion, we selected 4000 °C·s^{-1} for our heating scans because, being the thermal lag small at this heating rate, it allows avoid thermal degradation of samples together with an optimal signal intensity.

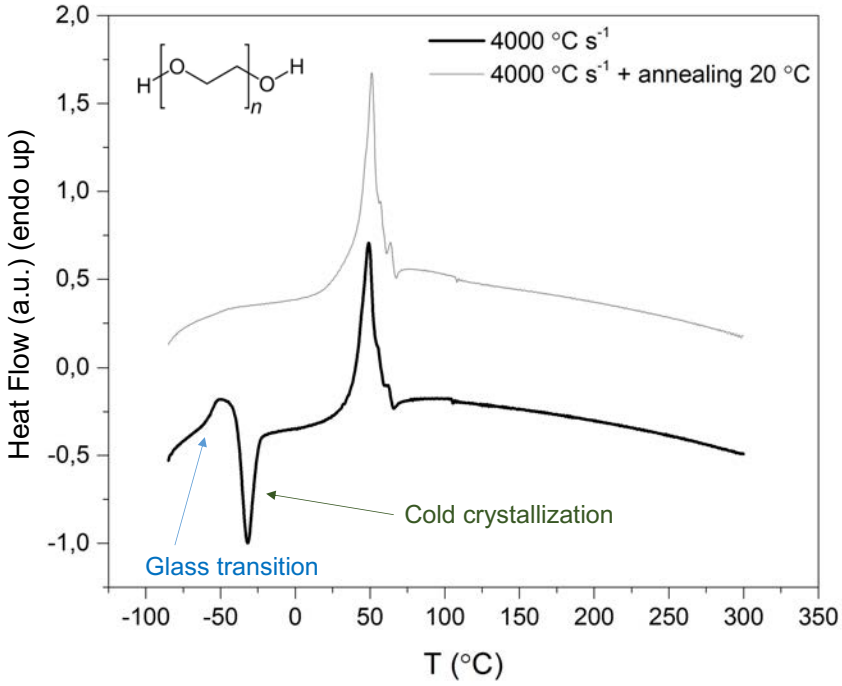

Figure S6. FSC heating scans for poly(ethylene oxide) (at 2000 ºC s^{-1}) after being cooled down from 300 ºC to -90 ºC at 4000 ºC s^{-1} (black line). The clear glass step-like signal of the glass transition is clearly seen in the heating scan, which means that -at least a significant fraction of- the material did not crystallize during cooling. For comparison, a heating scan (at 2000 ºC s^{-1}) of a crystalline PEO sample is also shown.

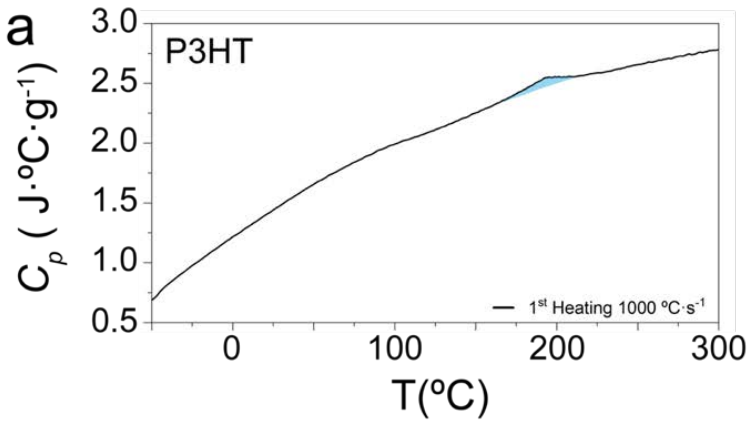

Figure S7. 1st heating scan (at 1000 ºC·s^{-1}) for a P3HT film spin-cast on the chip sensor from chloroform.

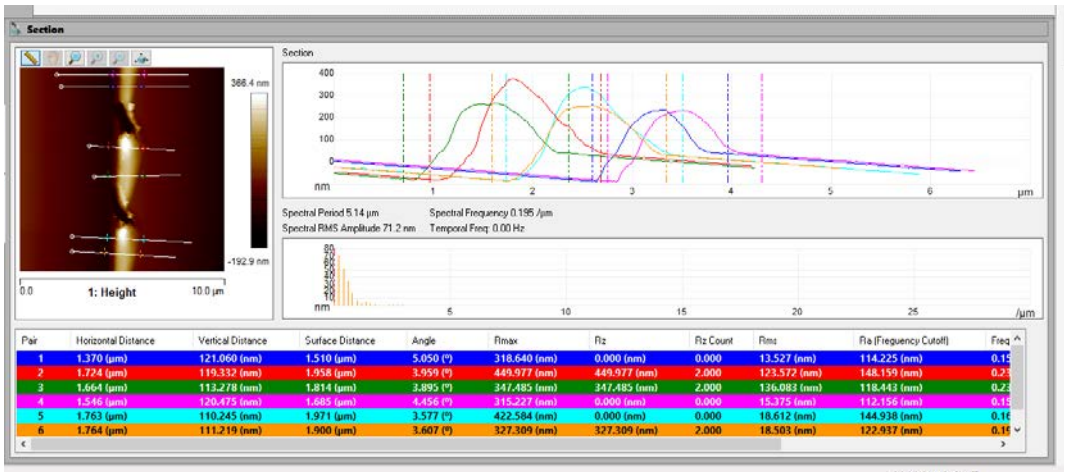

Figure S8. AFM scratch analysis of PBDB-T thin films. Film thickness was evaluated from height profiles.

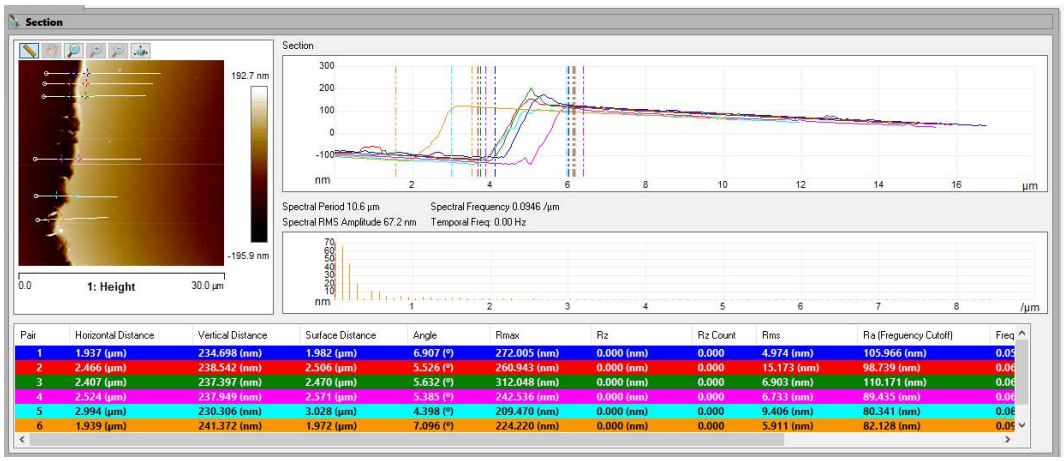

Figure S9. AFM scratch analysis of PBDB-T-2F thin films. Film thickness was evaluated from height profiles.

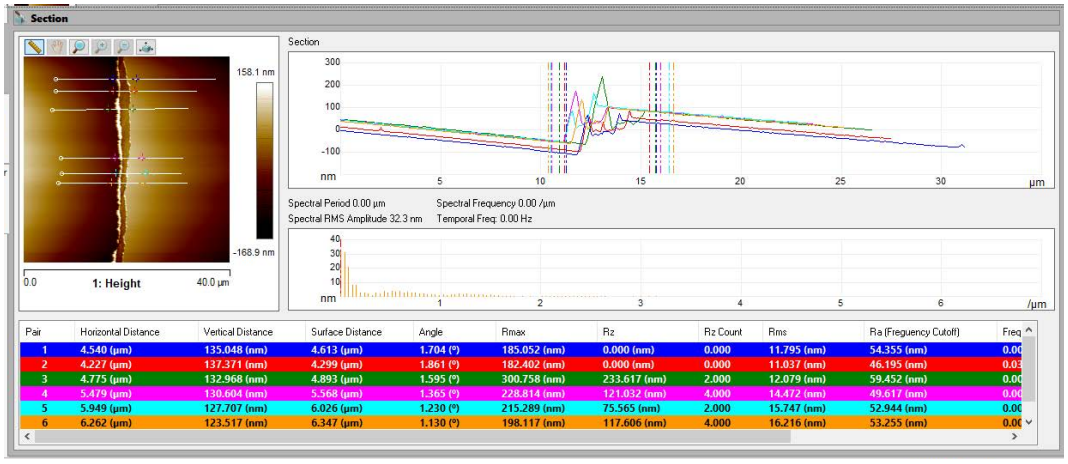

Figure S10. AFM scratch analysis of PBDB-T-2Cl thin films. Film thickness was evaluated from height profiles.

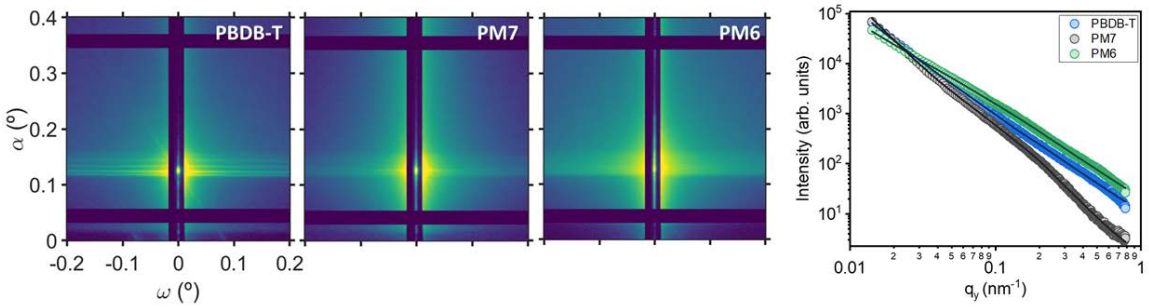

Figure S11. GISAXS patterns of PBDB-T, PM7 and PM6 at a grazing angle of 0.12°, and (right) the horizontal cuts at Yoneda Peak, together with their corresponding fitted curves.

The GISAXS patterns were analyzed by extracting horizontal cuts nearly at the Yoneda peak. The intensity profiles, in function of q_y, are compared (Figure S10) and fitted using the Unified model by Beaucage ((G. Beaucage, *J. Appl. Crystallogr*. 1995, 28, 717.).). The three samples yield intense scattering patterns due to a high electronic contrast at ranges between 10-100 nm. Since the patterns come from one single material, we associate this intensity to the density difference between small crystalline clusters and more disordered regions. However, the horizontal cuts from Figure S10 do not display any clear peak or shoulder, suggesting a high polydispersity of sizes and lack of correlation between the crystalline regions. The Unified model by Beaucage allows us to extract an average radius of gyration of these structures: 23 nm for PBDB-T and PM7 and 29 nm for PM6. These numbers are in the same scale range as the data extracted from AFM.

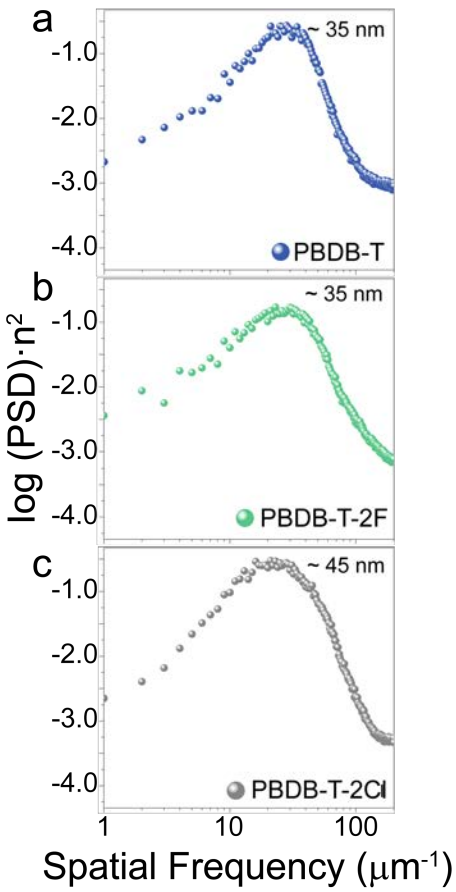

Figure S12. Power spectral density (PSD) curves.

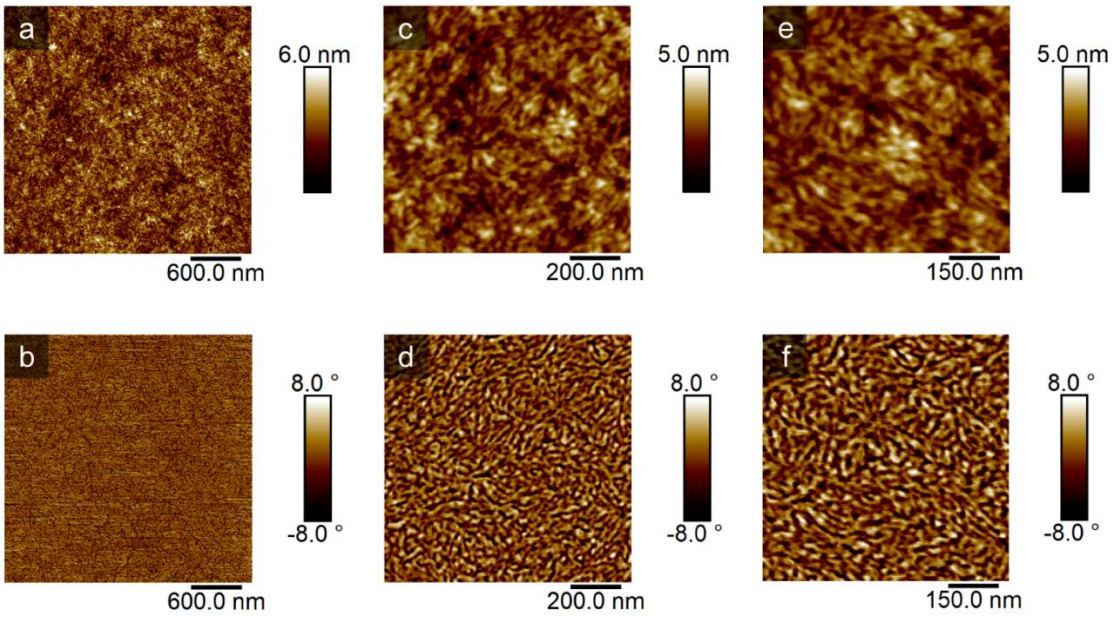

Figure S13. AFM topography and phase images for a PBDB-T thin film

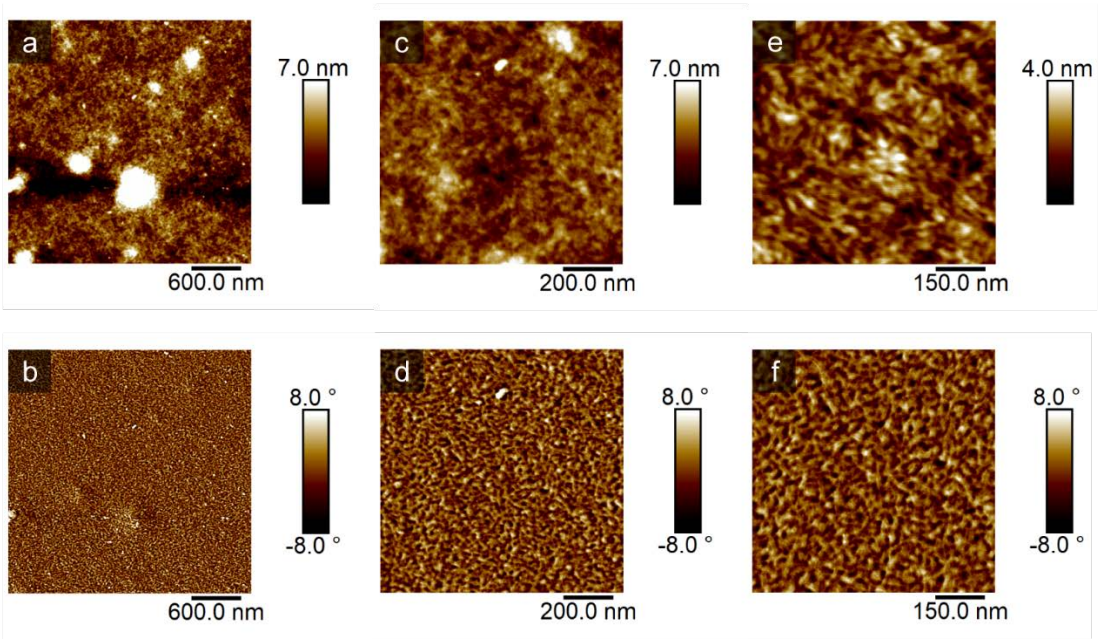

Figure S14. AFM topography and phase images for a PBDB-T-2F thin film

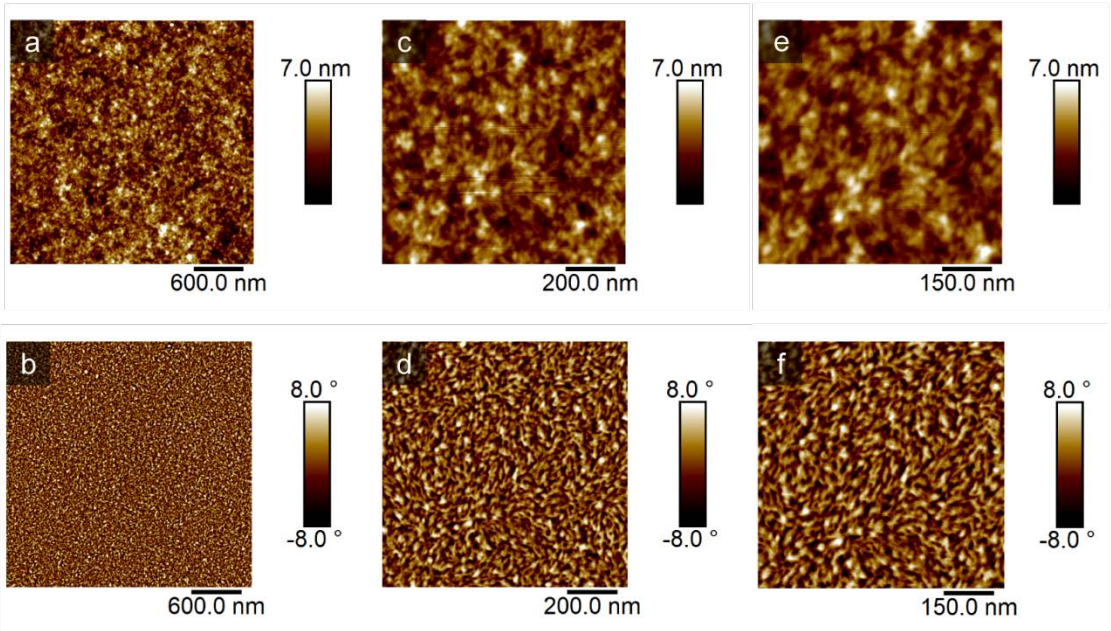

Figure S15. AFM topography and phase images for a PBDB-T-2Cl thin film

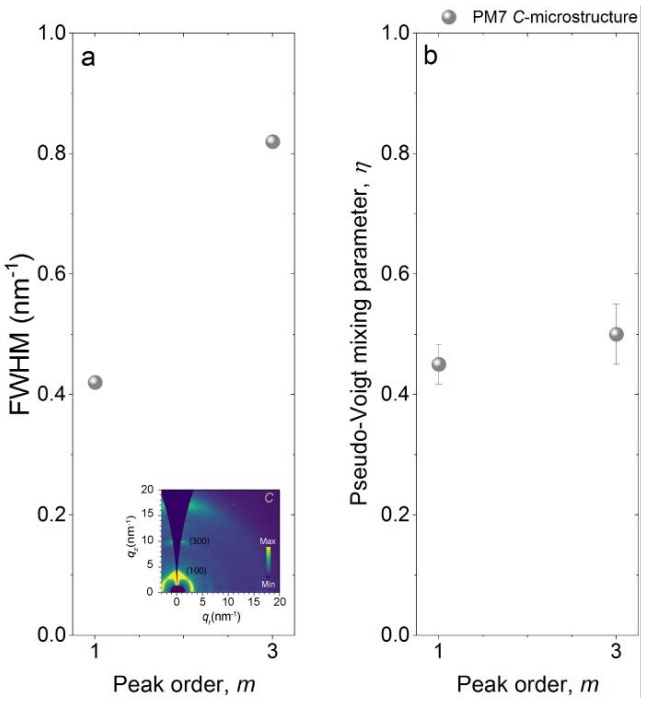

Figure S16. Peak parameters determined from 100 and 300 peak of PBDB-T-2Cl in C-microstructure. (a) Peak full width half maximum as a function of peak order and (b) Pseudo-Voigt mixing parameter, η, as a function of peak order.

Peak shape analysis of the *(100)* and *(300)* reflections was performed to gain insights into the paracrystalline nature of the lamellar stacking. Additionally, the width of *(100)* and *(300)* separated peaks was calculated and the trend as a function of peak order was observed.[2]

The relative constant values of pseudo-Voigt mixing parameter between 0 and unity indicate that both paracrystalline disorder and lattice parameter fluctuation are relevant for peak width. However, an increase in peak width with order informs that peak width is mainly governed by paracrystalline disorder.[3]

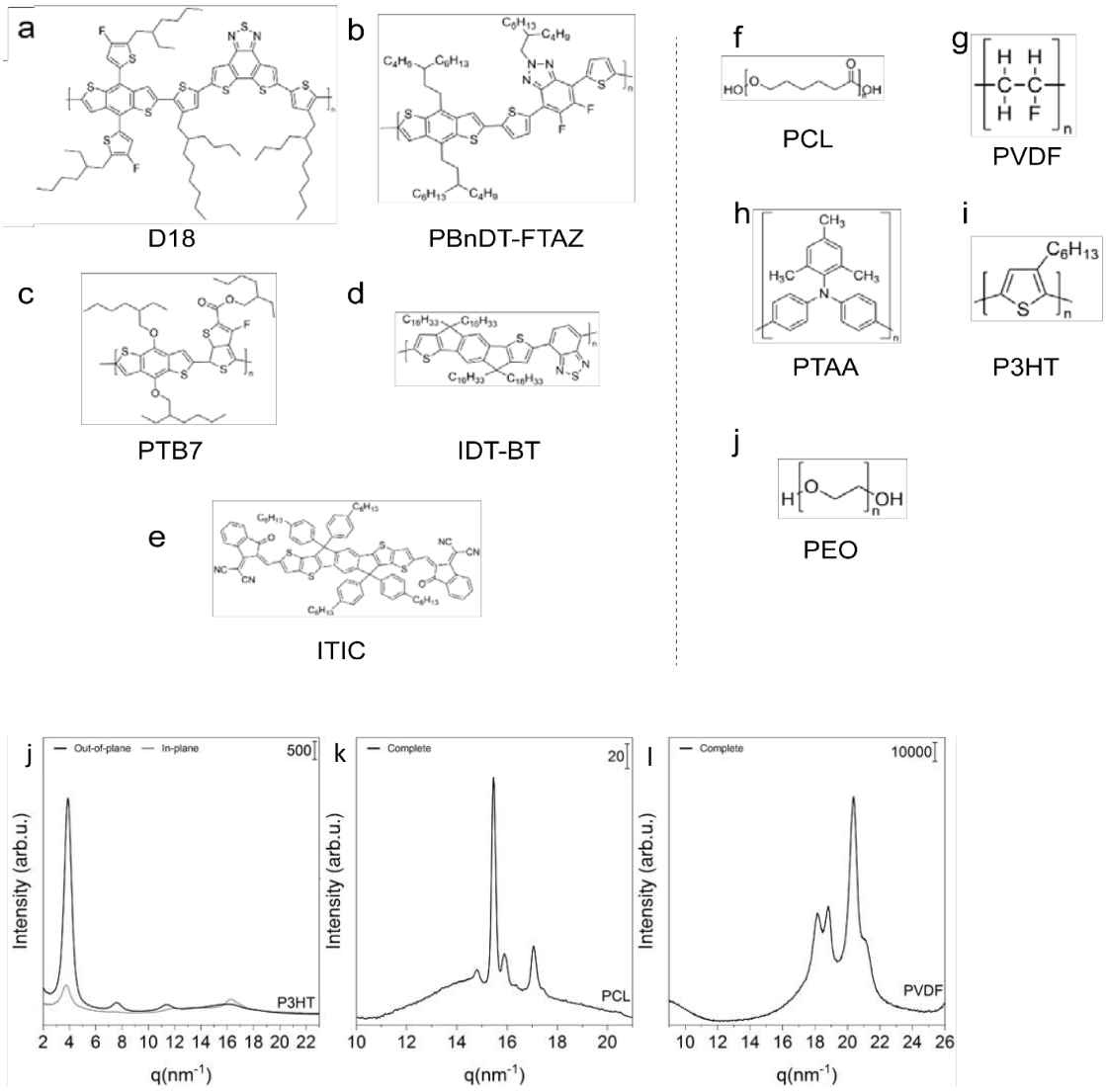

Figure S17 Molecular structures of (a) D18, (b) PBnDT-FTAZ, (c) PTB7, (d) IDT-BT, (e) ITIC, (f) PCL, (g) PVDF, (h) PTAA, (i) P3HT. GIWAXS 1D patterns for P3HT, PCL and PVDF.

Discussion on IDT-BT

"In order to assess the applicability of the semi-paracrystalline organization to high mobility polymers, IDTB-T films (drop cast from o-dichlorobencene) were investigated by GIWAXS and FSC (Figure S16). The estimated paracrystalline distortion parameter for the (010) peak, g_{010}, was found to be ~21%, i.e. similar to the ones obtained for PBDB-T family of polymers. We must note, however, that the (010) peak seems to be here convoluted with the isotropic amorphous halo, which most probably results in an artificial broadening of the (010) peak. We must also note that the large amount of diffuse scattering from disordered regions in the pattern can indicate that the IDTBT films contain a larger fraction of non-paracrystalline, disordered material than PM6, PBDB-T and PM7.

The first heating thermogram of drop cast IDTBT, recorded by FSC at 4000 $ºC \cdot s^{-1}$ revealed an endothermic process at about 250 ºC. This is well-above the glass transition temperature of disordered regions in this polymer materials (which according to our data is about 160 ºC). Therefore, the endothermic peak of the FSC pattern is compatible, here again, with the melting of paracrystallite units.

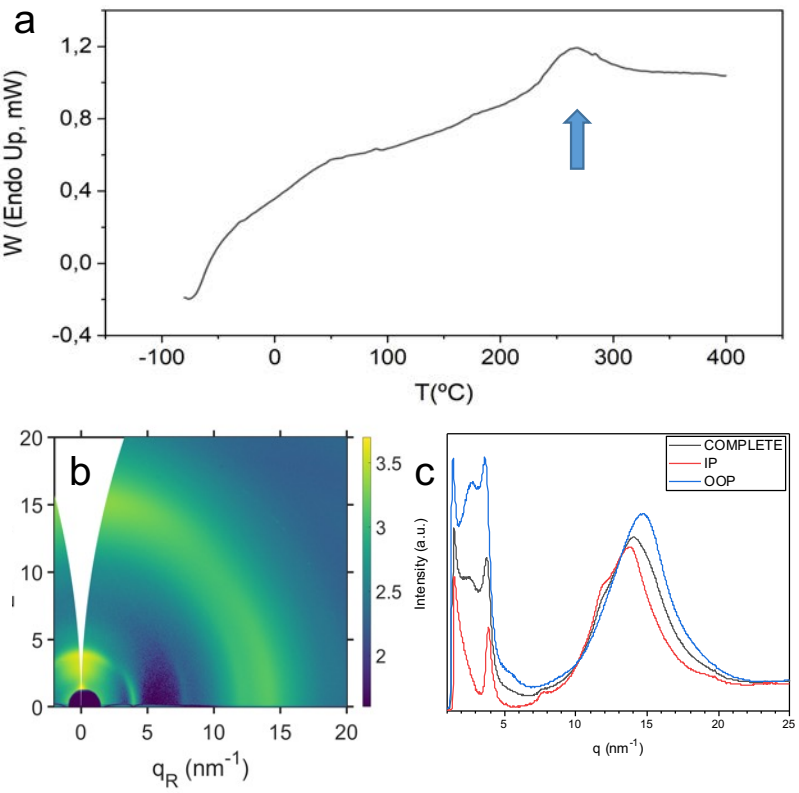

Figure S18. (a) FSC heating trace (at 4000 K/s), (b) 2D-GIWAXS pattern and (c) GIWAXS profiles for drop cast IDTB-T.

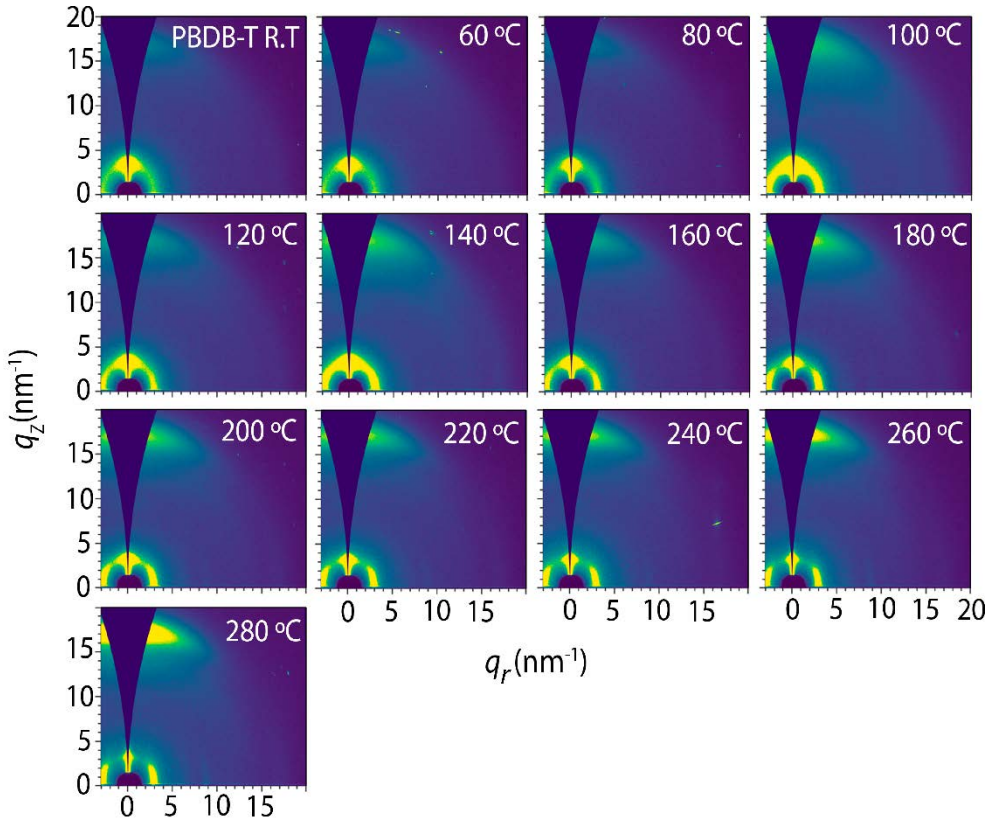

Figure S19. **(a)** 2D ex-situ GIWAXS patterns after annealing PBDB-T films at specified temperature during 10 minutes.

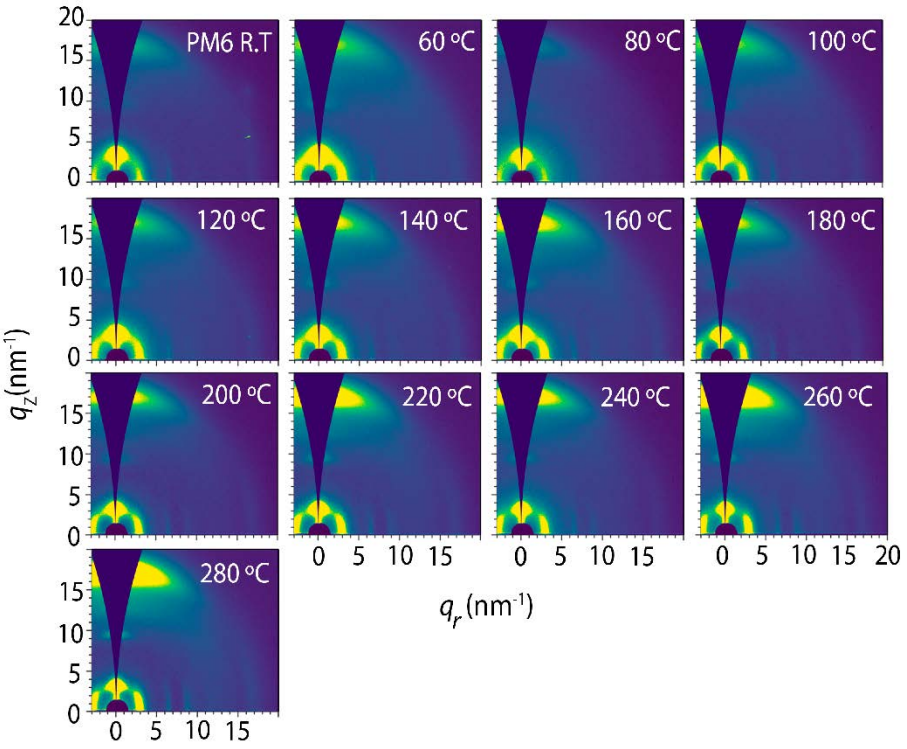

Figure S20. **(a)** 2D ex-situ GIWAXS patterns after annealing PBDB-T-2F films at specified temperature during 10 minutes.

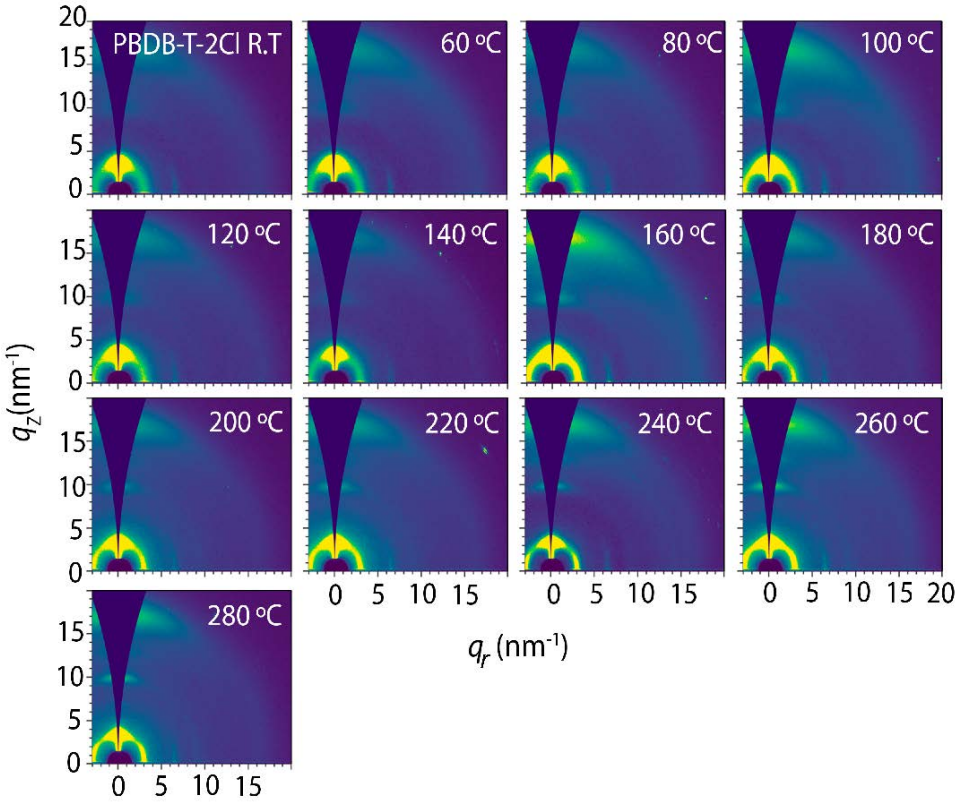

Figure S21. **(a)** 2D ex-situ GIWAXS patterns after annealing PBDB-T-2Cl films at specified temperature during 10 minutes.

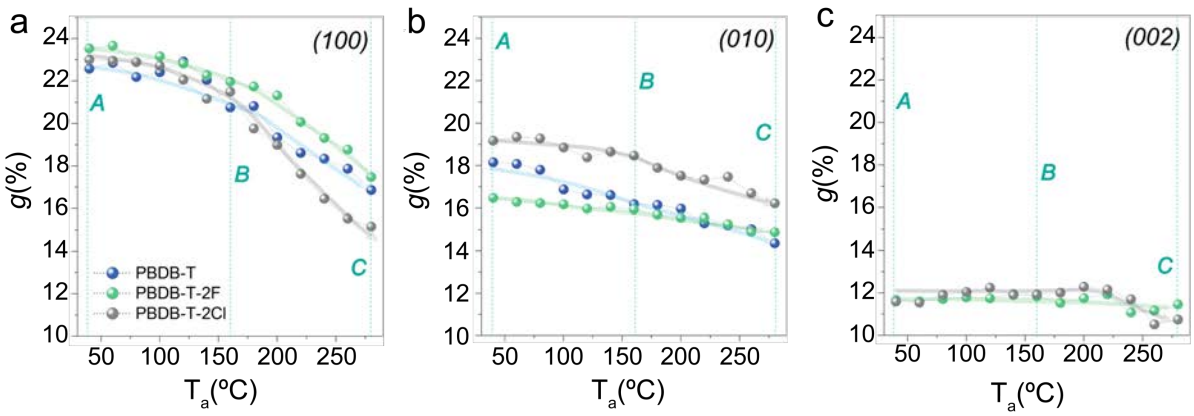

Figure S22 Paracrystalline distortion parameter, g, for the (100) (a), (010) (b) and (002) (c) planes as a function of the annealing temperature, Ta, for PBDB-T, PBDB-T-2F and PBDB-T-2Cl.

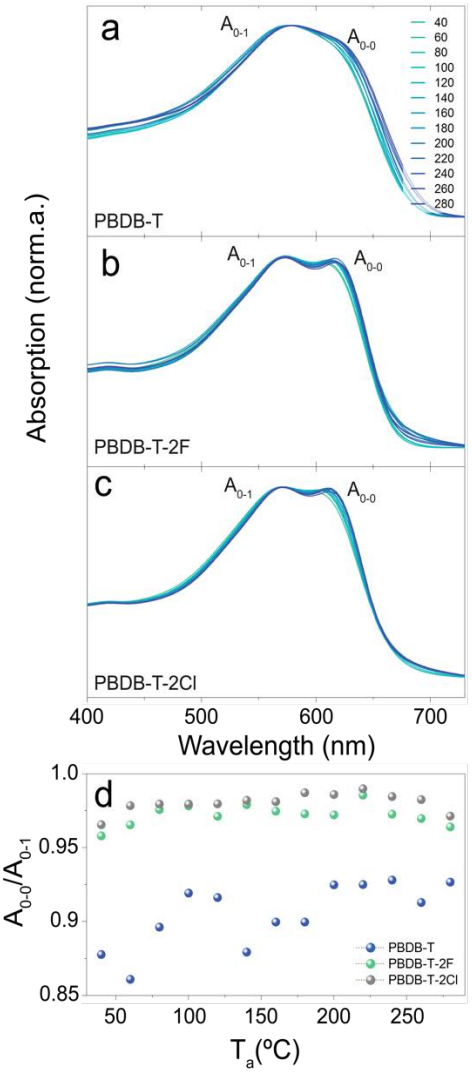

Figure S23. UV-vis absorption spectra for (a) PBDB-T, (b) PBDB-T-2F and (c) PBDB-T-2Cl films annealed at different temperatures. (d) Ratio between the intensities of the bands corresponding to the 0-0 transition (at ~610 nm) and the 0-1 transition (~570 nm).

Because the spectral features of photogenerated excitons, i.e. optical absorption, are linked to molecular conformation and arrangement, the relationships between optical

properties and the solid-state microstructure for PBDB-T, PBDB-T-2F and PBDB-T-2Cl can be studied by UV-vis spectroscopy (UV-vis spectra were recorded with a Shimadzu UV-2550 spectrometer with a film adapter). UV-vis spectra recorded for films annealed at different T_as in the range between 40 ºC and 280 ºC are shown in (Figure S23). In general, we found that the vibronic structure is less distinctive for PBDB-T than for PBDB-T-2F and PBDB-T-2Cl. Moreover, the ratio between the intensities of the bands corresponding to the transition to the lowest vibronic level (i.e. the 0-0 transition at ~610 nm) and the transition to the next vibronic level (i.e. the 0-1 transition at ~570 nm), A_{0-0}/A_{0-1}, has a greater value for PBDB-T-2F and PBDB-T-2Cl than for PBDB-T (Figure S23d). Because A_{0-0}/A_{0-1} can be employed to parametrize the intrachain optoelectronic coupling of neighboring chromophores,[1,2] a higher A_{0-0}/A_{0-1} value is typically interpreted as a greater abundance of chain segments with planarized conformations, which is often interpreted as a higher conformational order of the material. Thus, our UV-vis results suggest that PBDB-T-2F and PBDB-T-2Cl exhibit, on average, a greater fraction of chains segments with planarized conformations than PBDB-T. However, in this case, a higher A_{0-0}/A_{0-1} seems not to be closely linked to a higher order of the paracrystalline microstructure. The evolution of the A_{0-0}/A_{0-1} ratio with the applied T_a is displayed in Figure S23

d. While the A_{0-0}/A_{0-1} ratio for PBDB-T exhibits a clear positive trend in the entire T_a range, that for PBDB-T-2Cl and PBDB-T-2F seems rather insensitive to T_a despite of the clear changes of the solid-state microstructure occurring when samples are thermally annealed. Indeed, a closer look at Figure S23d reveals the lowering of the A_{0-0}/A_{0-1} ratio when the highest T_as are applied even if the degree of crystallinity and the size of crystals are enhanced and the g decreases at these T_as. The advance of the degree of

paracrystallinity and the decrease of the paracrystalline disorder in PBDB-T-2Cl and PBDB-T-2F certainly result in the ordering of backbone chains, but also involve the improvement of the intermolecular arrangements via π-π staking, which seems to promote H-aggregation, decreasing the $A_{0\text{-}0}/A_{0\text{-}1}$ ratio.

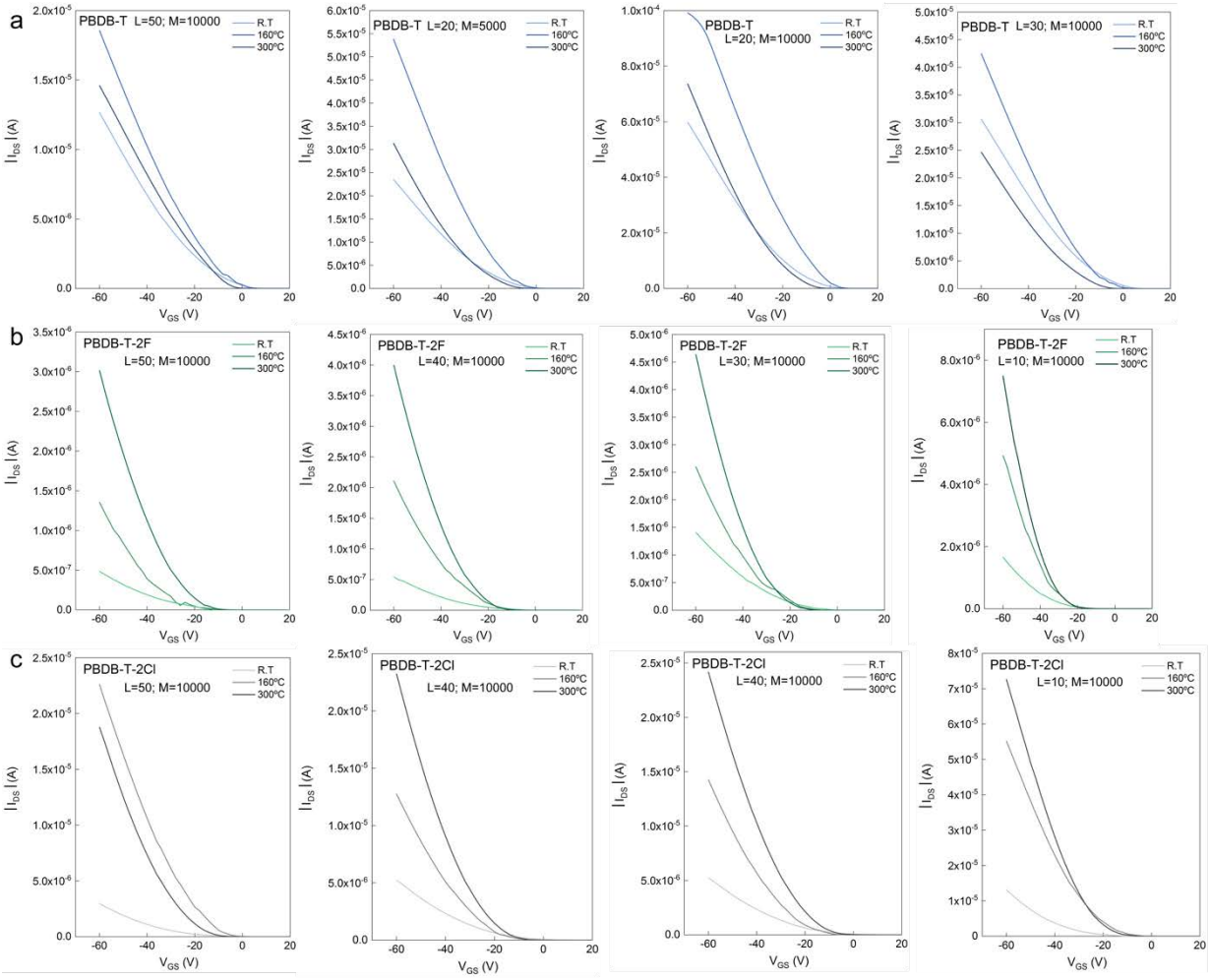

Figure S24. Transfer characteristics of more devices for (a) PBDB-T, (b) PBDB-T-2F and (c) PBDB-T-2Cl field effect transistors annealed at 25 °C, 160 °C and 280 °C. Width and length are specified in each graph; in all cases VDS= - 60 V.

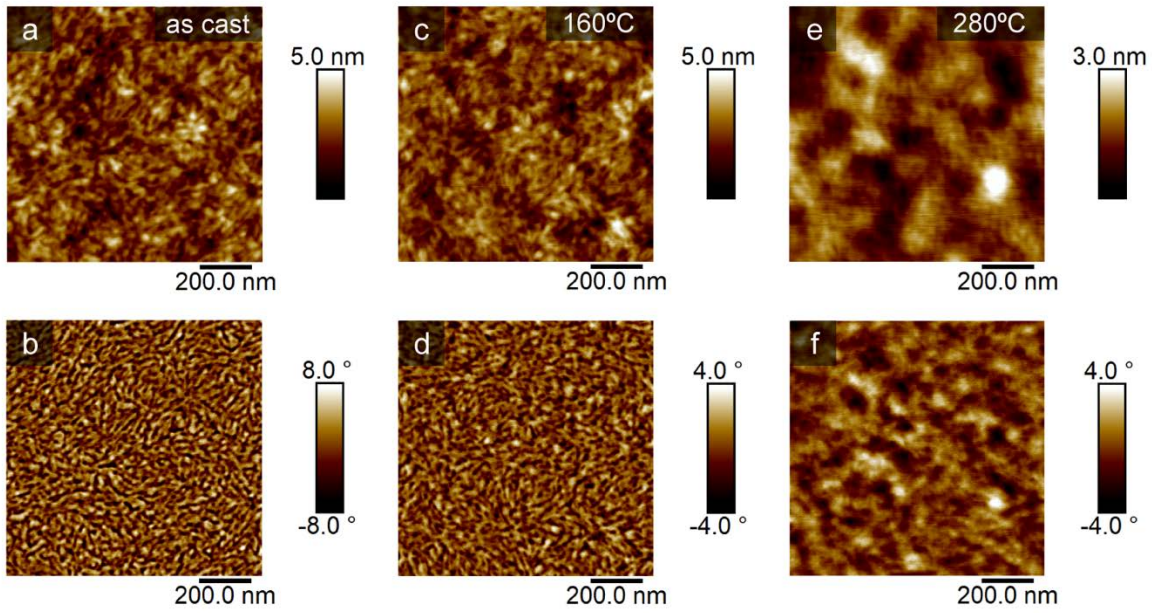

Figure S25. AFM topography and phase images for a PBDB-T thin film annealed during 10 minutes. Temperatures are labelled on top of the image **(a-b)** without annealing, **(c-d)** annealed at 160°C, and **(e-f)** annealed at 280°C.

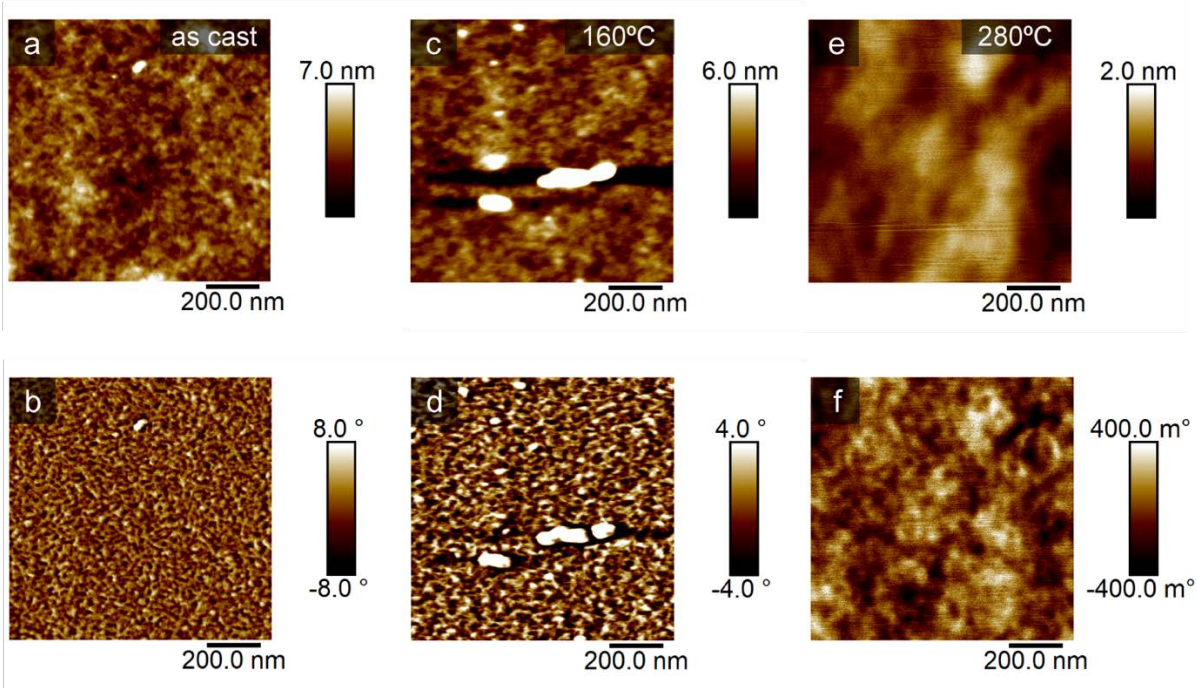

Figure S26. AFM topography and phase images for a PBDB-T-2F thin film annealed during 10 minutes. Temperatures are labelled on top of the image **(a-b)** without annealing, **(c-d)** annealed at 160°C, and **(e-f)** annealed at 280°C.

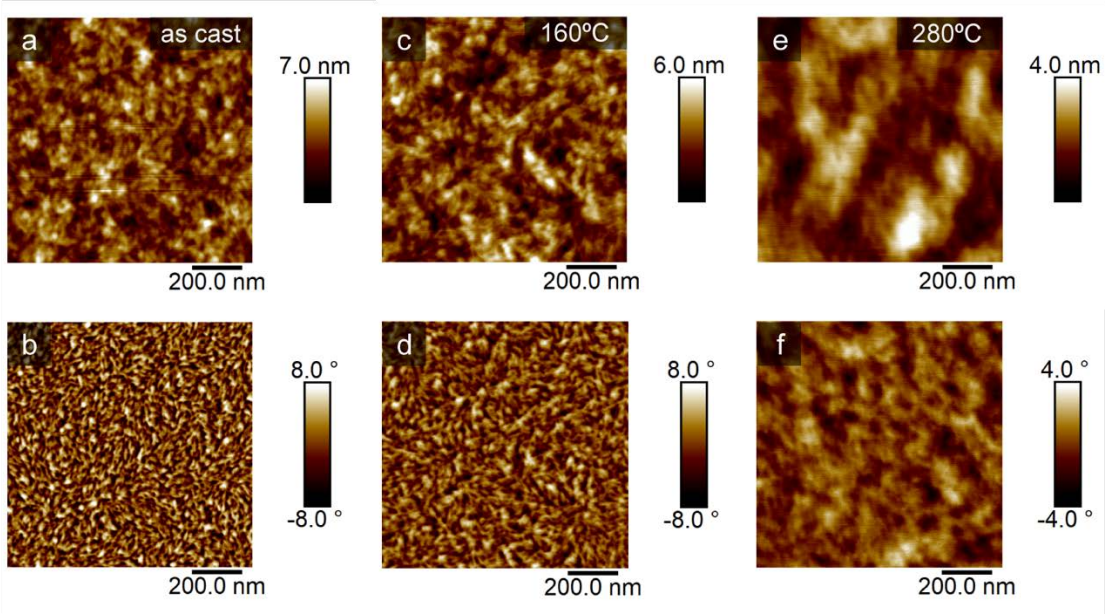

Figure S27. AFM topography and phase images for a PBDB-T-2Cl thin film annealed during 10 minutes. Temperatures are labelled on top of the image **(a-b)** without annealing, **(c-d)** annealed at 160°C, and **(e-f)** annealed at 280°C.

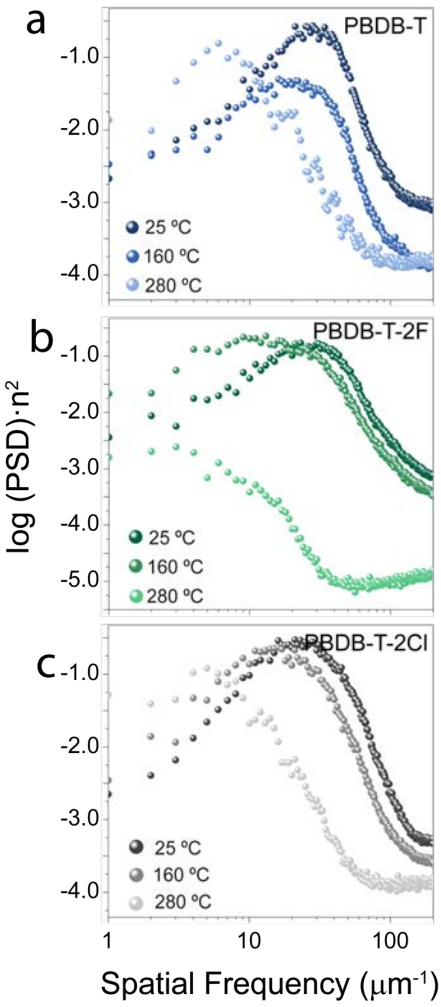

Figure S28 Power spectral density (PSD) curves of AFM phase contrast images.

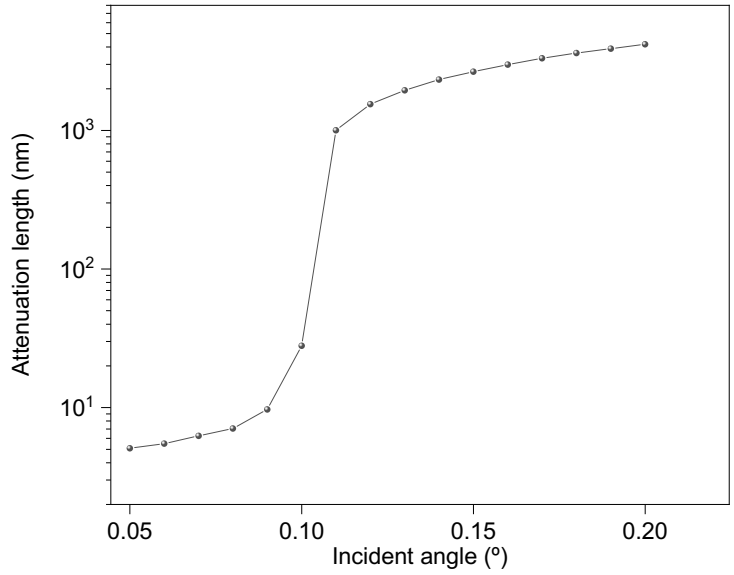

Figure 29. Profile of the attenuation length vs incident angle for a PBDB-T film.

Prior to our GIWAXS analysis, we evaluated the penetration (in fact, the attenuation) of the X-ray beam (considering the X-ray refractive index of the materials and the energy of the beam) employing a software from Lawrence Berkeley National Laboratory's (LBNL) (https://henke.lbl.gov/optical_constants/atten2.html). The outcome is summarized in the plot shown below: As can be clearly seen, the attenuation length, i.e. the depth into the material measured along the surface normal where the intensity of x-rays, increased up to 1 micrometer for incident angles >0.11º. This means that using an incident angle of 0.12º, like in our experiments, the X-ray beam could penetrate and probe the whole volume of the film.

Parameters used of the simulation:

Energy = 12.4 KeV (0.1 nm)
Chemical formula: C68H78O2S8 (PBDB-T)
Density = 1.1 g/cm3
Source: https://henke.lbl.gov/optical_constants/atten2.html

Moreover, in order to double-check the above, we have repeated our GIWAXS experiments employing an incident angle of 0.2º, i.e. well-above the critical angle of polymer materials (and above the critical angle of Si substrates). In the figure below (which is also included in the supporting information Figure 29) we have compared our previous data (obtained with angles of 0.12-0.15º) with the new set of data at 2º. Clearly, the comparison evidences no differences between results at 0.12-0.15 and 0.2º.

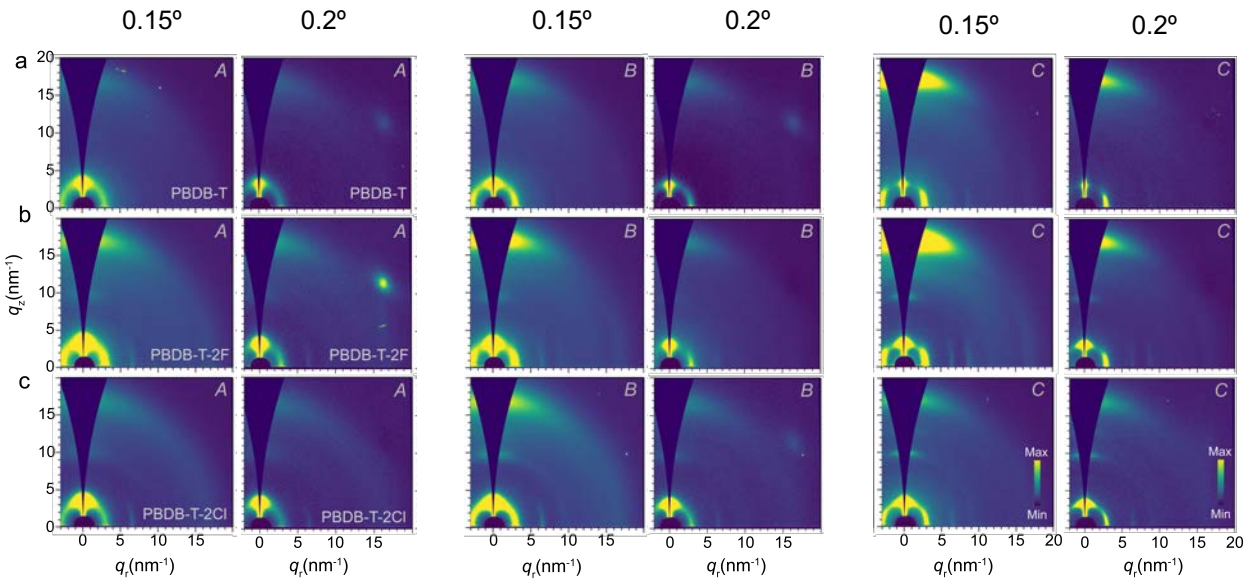

Figure S30. Comparison between GIWAXS results recorded with incident angles of 0.15º and 0.2º, for PBDB-T, PM6 and PM7 in the so-called microstructures A, B and C.

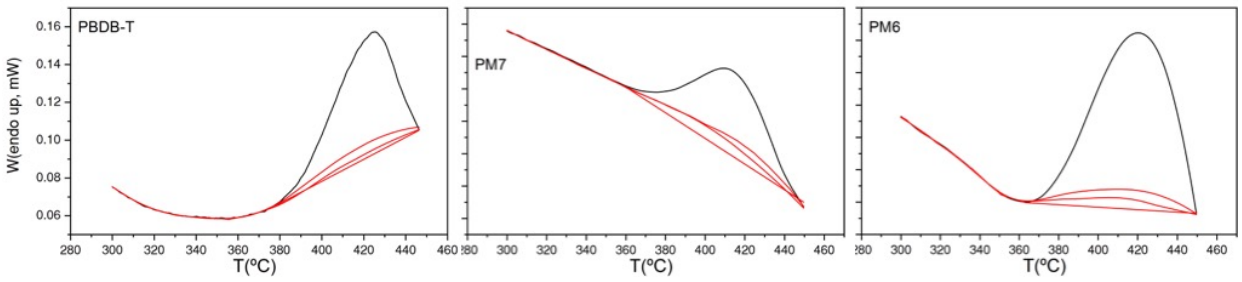

Figure 31. Different baselines considered for the error calculation in the measurement of Errors in the measurement of ΔH_f